Article

Formative Period Tracing and Driving Factors Analysis of the Lashagou Landslide Group in Jishishan County, China

Qianyou Fan [1], Shuangcheng Zhang [1,2,*], Yufen Niu [3], Jinzhao Si [1], Xuhao Li [1], Wenhui Wu [1], Xiaolong Zeng [1] and Jianwen Jiang [1]

[1] College of Geological Engineering and Geomatics, Chang'an University, Xi'an 710054, China; 2020026013@chd.edu.cn (Q.F.); 2020126029@chd.edu.cn (J.S.); 2022126034@chd.edu.cn (X.L.); 2021226025@chd.edu.cn (W.W.); 2022126035@chd.edu.cn (X.Z.); jjw@chd.edu.cn (J.J.)

[2] Observation and Research Station of Ground Fissure and Land Subsidence, Ministry of Natural Resources, Xi'an 710054, China

[3] School of Mining and Geomatics Engineering, Hebei University of Engineering, Handan 056038, China; niuyufen@hebeu.edu.cn

* Correspondence: shuangcheng369@chd.edu.cn

Abstract: The continuous downward movement exhibited by the Lashagou landslide group in recent years poses a significant threat to the safety of both vehicles and pedestrians traversing the highway G310. By integrating geomorphological interpretation using multi-temporal optical images, interferometric synthetic aperture radar (InSAR) measurements, and continuous global navigation satellite system (GNSS) observations, this paper traced the formation period of the Lashagou landslide group, and explored its kinematic behavior under external drivers such as rainfall and snowmelt. The results indicate that the formation period can be specifically categorized into three periods: before, during, and after the construction of highway G310. The construction of highway G310 is the direct cause and prerequisite for the formation of the Lashagou landslide group, whereas summer precipitation and spring snowmelt are the external driving factors contributing to its continuous downward movement. Additionally, both the long-term seasonal downslope movement and transient acceleration events are strongly controlled by rainfall, and there is a time lag of approximately 1–2 days between the transient acceleration and heavy rainfall events. This study highlights the benefits of leveraging multi-source remote sensing data to investigate slow-moving landslides, which is advantageous for the implementation of effective control and engineering intervention to mitigate potential landslide disasters.

Keywords: shallow loess landslide; slope excavation; multi-source remote sensing; evolutionary history; triggering factors

check for updates

Citation: Fan, Q.; Zhang, S.; Niu, Y.; Si, J.; Li, X.; Wu, W.; Zeng, X.; Jiang, J. Formative Period Tracing and Driving Factors Analysis of the Lashagou Landslide Group in Jishishan County, China. *Remote Sens.* **2024**, *16*, 1739. https://doi.org/10.3390/rs16101739

Academic Editors: Federico Raspini, Chao Zhou and Kunlong Yin

Received: 10 April 2024
Revised: 7 May 2024
Accepted: 7 May 2024
Published: 14 May 2024

1. Introduction

In recent years, with the progressive implementation of the Western Development Drive Strategy, China has constructed several high-level mountain roads. However, the frequent excavation of hillsides during construction disrupts the stress balance of the original slope, subsequently triggering a series of landslides [1]. Conducting research on the long-term kinematic characteristics and causative factors of landslides is crucial for implementing focused monitoring, early warning, and engineering interventions, ultimately reducing the disaster risk to a socially acceptable level.

Optical remote sensing enables the reproduction of the kinematic behavior of fast-moving landslides through the visual interpretation of surface geomorphological features [2,3]. For instance, Lacroix et al. [2] investigated the reactivation of the Harmalière landslide using Sentinel-2 optical data. The results revealed a 7-month period of low activity (≤ 1 m), followed by a sudden acceleration of 3.2 ± 1.2 m in 3 days, before the failure of a mass of about 2 to 3.6×10^6 m^3. However, the method faces challenges in capturing the kinematic characteristics and stability of slow-moving landslides (ranging from mm/year to cm/year) due to the limitations of meter-level spatial resolution and temporal resolution related to cloud cover [4,5]. In contrast, InSAR technology facilitates all-day and all-weather observations with high accuracy, measuring from centimeters to millimeters [6–9]. With this technology, it becomes possible to capture the surface kinematic characteristics of landslides at a spatial scale, ranging from several meters to tens of meters [10]. In addition, massive synthetic aperture radar (SAR) data archived over the past 30 years have made it possible to retrieve the long-term spatiotemporal kinematic characteristics of landslides [11,12]. For example, Cignetti et al. [13] investigated the 26-year spatiotemporal evolution of Sauze d'Oulx slopes using four different datasets, ERS 1/2, Radarsat-1/2, COSMO SkyMed, and Sentinel-1, collected between 1992 and 2018. Xu et al. [14] retrieved the 12-year kinematic characteristics of Hooskanaden landslide from 2007 to 2019 by combining digital elevation model (DEM), ALOS-1/2, and Sentinel-1 datasets.

Due to the SAR satellite's revisited period, which ranges from several days to tens of days, the InSAR technology faces challenges in capturing the instantaneous response of landslide dynamics to external environmental factors like rainfall, mountain fires, and so forth [15–17]. GNSS technology, with its ability to continuously track Earth's surface displacements in real time at a high sampling rate (seconds or less), is a valuable tool for studying the kinematic behavior of landslides and analyzing the impact of external triggers [18,19]. Therefore, combining continuous GNSS measurements with high temporal resolution and spaceborne InSAR measurements with high spatial resolution can potentially reveal more comprehensive insights into the kinematic characteristics and deformation mechanisms of landslides [20–22]. For instance, Hu et al. [23] successfully delineated the intricate spatiotemporal variations in the kinematic characteristics of the Crescent Lake landslide by integrating data from semi-permanent GNSS stations with space-borne InSAR measurements. Moreover, they established a threshold for the amount of pre-accumulated rainfall needed to trigger the displacement of the landslide.

The Lashagou landslide group is situated in the transitional zone between the Qinghai–Tibet Plateau and the Loess Plateau (Figure 1a). Its primary cause of formation is considered to be the hillslope excavation activities conducted during the construction of the highway G310 from 2011 to 2013 [10,24]. However, no studies have yet demonstrated the impact of the construction of the highway G310 on the formation and evolution of the Lashagou landslide group. The latest research indicates that the Lashagou landslide group remained in a state of continuous downward movement from 2020 to 2021 [24], posing a significant threat to the safety of both vehicles and pedestrians on highway G310. To exacerbate the situation, a magnitude 6.2 earthquake transpired on 18 December 2023, at a distance of approximately 18 km from the Lashagou landslide group (Figure 1a). This unfortunate occurrence resulted in the tragic loss of 151 lives and induced a minimum of 3767 co-seismic landslides [25]. The research conducted by Huang et al. [26] and Liu et al. [27] indicates that the Lashagou landslide group is situated in an area highly susceptible to post-earthquake geological disasters. Therefore, the Lashagou landslide group poses a significant risk of failure during the approaching spring snowmelt season and rainy season.

Taking the Lashagou landslide group as a case study, this research examines the collaborative use of various remote sensing technologies to investigate the kinematic characteristics and driving factors influencing landslides. We firstly employed geomorphological interpretation using multi-temporal optical images and small baseline subset InSAR (SBAS-InSAR) technology to trace the formation period of the Lashagou landslide group and analyze the impact of the construction of highway G310 on its spatiotemporal evolution patterns. Meanwhile, the characteristics and mechanisms of landslide downward movement were analyzed based on InSAR time-series displacement over a period of 9 years. Finally, the kinematic behavior of the Lashagou landslide group, including seasonal variations, transient acceleration events, and episodic failure events, was investigated by GNSS measurements with high temporal sampling frequency. This study highlights the benefits of leveraging multi-source remote sensing data to investigate slow-moving landslides, which is advantageous for the implementation of effective control and engineering intervention to mitigate potential landslide disasters.

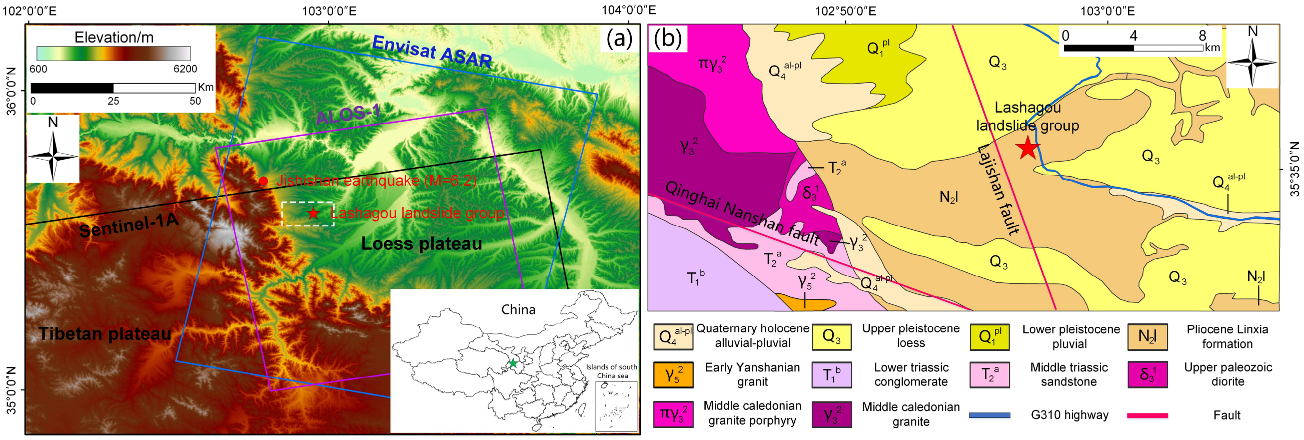

Figure 1. (**a**) Location of the study area and spatial coverage of the SAR data used in this study. The green star in the inset represents the geographical location of the Lashagou landslide group in China. (**b**) Regional engineering geological map of the study area (the dotted white area in (**a**)). The red star denotes the location of the Lashagou landslide group.

2. Study Area

Jishishan County is located in the transition zone between the Qinghai–Tibet and the Loess plateaus (Figure 1a), with mountainous terrain accounting for approximately 90% of the total area [28]. The active tectonic movement in the northeastern Qinghai–Tibet Plateau and the weak strata (high porosity and low cohesion of loess material, which makes it easily erodible and prone to collapse under pressure) of the Loess Plateau have made Jishishan County one of the regions with the most serious geological disasters in China [29]. The Lashagou landslide group, located in the southern region of Jishishan County, consists of eight small- and medium-sized landslides (Figure 2a). The average gradient where the landslide group is located measures approximately 19.5°, while the gradient at the foot ranges between 50° and 80° (e.g., steep free surface in Figure 2b,c). In addition, the landslide group is primarily distributed at an elevation ranging from 1100 m to 1200 m. Of these, the L1 landslide holds the title of being the largest, covering an area of approximately 49,600 m^2, while the L8 landslide is identified as the smallest, encompassing a mere 2900 m^2.

The surrounding area of the landslide group is widely distributed in Quaternary aeolian loess (Q_3), alluvial loess (Q_4^{al-pl}), and Neogene sand-mudstone (N_2I) from the Linxia Formation [10]. The area also features exposed strata from the Sinian, Carboniferous, Permian, and Cretaceous (Figure 1b). According to the borehole data, the sliding surface is situated at the interface of loess and silty clay (Figure 3). The sliding body primarily comprises Pliocene silty loess (Figure 3b), characterized by loose porosity and well-developed vertical joints, resulting in strong permeability. The underlying strata are composed of Middle Pleistocene silty clay (Figure 3b), which is mostly impermeable or weakly permeable mudstone. The differential permeability characteristics between the loess and clay strata create favorable conditions for the formation and subsequent development of the Lashagou landslide group [10,30].

According to records from the Jishishan County People's Government (http://www.jss.gov.cn/ (accessed on 8 March 2023)), the Jishishan region is characterized by a typical continental monsoon climate, featuring an average annual precipitation of 660.2 mm and an average annual evaporation of 880 mm. The majority of rainfall is concentrated from May to August, encompassing around 60–78% of the annual precipitation, often accompanied by heavy rain events. Located within the seasonal permafrost zone, the region experiences a winter extreme minimum temperature of −32.2 °C, with a maximum freezing depth of

1.2 m. Significantly, the initial freezing of the landslide surface loess typically occurs around mid-November each year, followed by a melting period from mid-February to early April, resulting in a high frequency of spring landslide disasters due to freeze–thaw erosion.

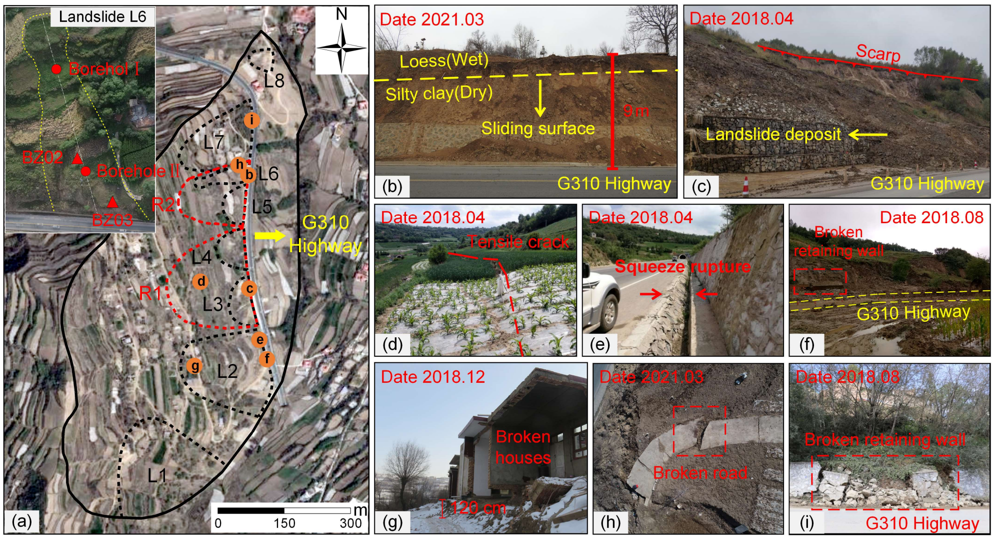

Figure 2. (**a**) Optical imagery of the Lashagou landslide group acquired from Google Earth. The red triangles and circles in the inset image are the locations of GNSS stations and boreholes, respectively. (**b**–**i**) Photos from the locations indicated by solid orange circles in (**a**), showing the damages caused by the landslides in 2018.

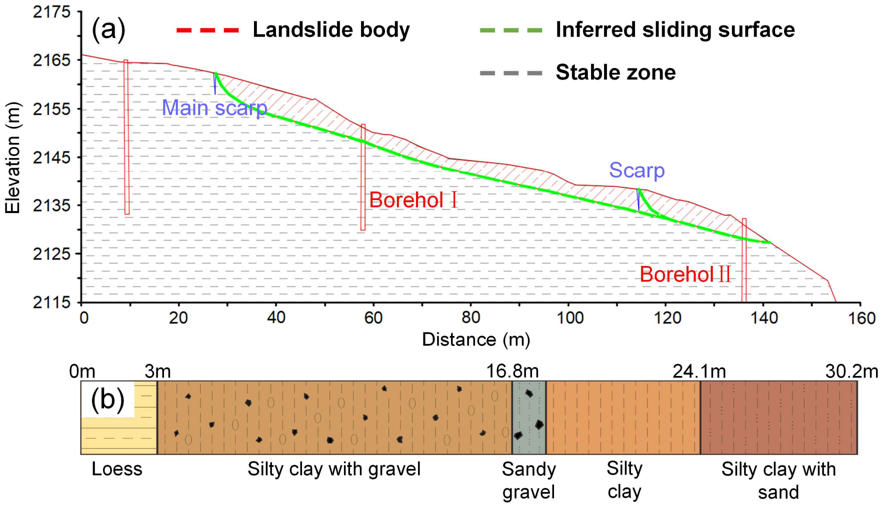

Figure 3. (**a**) Engineering geological profile of the L6 landslide, whose location is illustrated in the inset image in Figure 2a. (**b**) Stratigraphy of borehole II.

As the primary route connecting Linxia City and Qinghai Province, the construction of highway G310 (Linxia section) began in January 2011 and opened to traffic in November 2013 (Figure 4). During this period, the slope where Lashagou Village was situated (represented by the solid black line in Figure 2a) was excavated to an average depth of 3–8 m and a maximum depth of 12 m [10]. Hillslope excavation led to a steep free surface of 50–80° on the left side of the highway (Figure 2a,b), which disrupted the initial stress equilibrium of the slope and ultimately led to the Lashagou landslide group. According to records from the Emergency Management Department of the Gansu Province, landslides L3 and L4 first occurred in early April 2018 (Figure 2c). These landslides expanded the damage to the upper slope during the subsequent rainy season (Figure 2d), ultimately leading to the formation of retrogressive landslide R1. Simultaneously, landslide L2 experienced accelerated displacement and continued to exert pressure on the retaining wall at its rupture surface, resulting in the uplift and crushing of the side ditch along the highway G310 (Figure 2e). On 2 and 3 August 2018, Jishishan County encountered an unusual rainstorm, with precipitation reaching as high as 194 mm [31]. This heavy rainfall directly triggered the landslide L2, causing damage to several houses and roads in Lashagou Village (Figure 2g). Additionally, the retaining wall at the foot of the slope was damaged (Figure 2f), leading to the closure of the highway for maintenance. Subsequently, landslide L1 suffered localized failure, but there were no associated casualties or property losses. Furthermore, several active landslides, i.e., L5, L6 (Figure 2h), and L7 (Figure 2i), were identified, whereas landslide L8 was classified as a failed landslide.

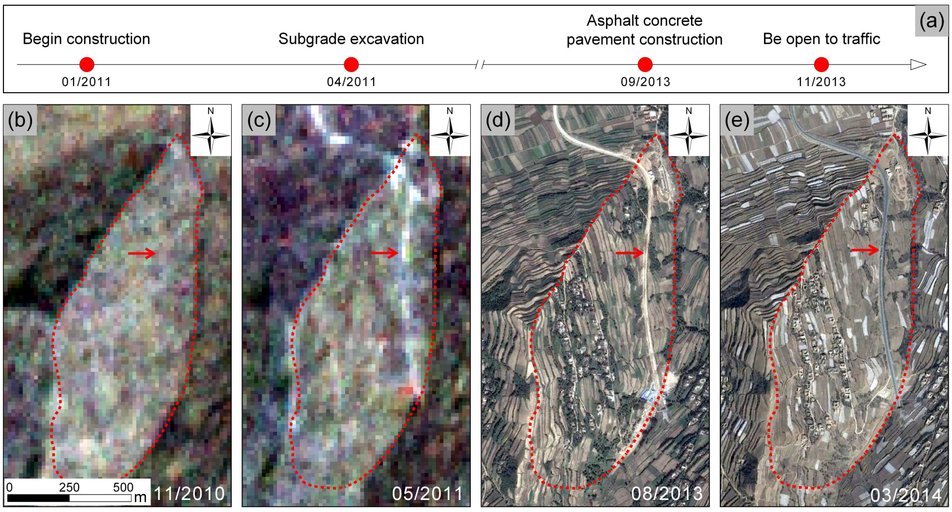

Figure 4. Optical satellite images recording the construction process of highway G310. (**a**) Important events during construction and their corresponding dates. (**b**,**c**) Landsat 7 images from November, 2010 and May, 2011. (**d**,**e**) Google Earth images from August 2013 and March 2014. The red dotted line indicates the extent of the slope where the Lashagou landslide group is located, and the red arrow points to highway G310.

3. Datasets and Methodology

3.1. Datasets

To reveal the long-term spatiotemporal evolution of the Lashagou landslide group, we analyzed three sets of SAR data with different imaging geometries acquired between 2006 and 2021. These datasets consisted of 26 descending Envisat images, 12 ascending ALOS-1 images, and 138 ascending Sentinel-1A images. Figures 1a and 5a show the spatial coverage and time span of the different SAR datasets, respectively, and Table 1 lists the fundamental parameters associated with the SAR datasets utilized in this study. In addition, four Google Earth historical images from September 2013, October 2015, November 2016, and October 2019, and an unmanned aerial vehicle (UAV) orthophoto image from August 2020 were used to reconstruct the spatiotemporal evolution history of the Lashagou landslide group.

The shuttle radar topography mission (SRTM) and ALOS world 3D (AW3D) DEMs with a resolution of 30 m were used to simulate and remove the topographic phase. Additionally, we employed UAV oblique photogrammetry to generate a high-precision DEM with a resolution of 0.05 m. Two GNSS stations (BZ02 and BZ03) installed on the landslide L6 (Figure 2a) provided 3D surface displacement with millimeter-level precision, which was used to validate the InSAR results and assist in time-series analysis. Rainfall and snowfall from 2006 onwards were provided by the Jishishan Meteorological Station, which is located approximately 14 km from the Lashagou landslide group. A soil hygrometer installed on landslide L6 measures the soil water content at a depth of 10 cm once every hour. In addition, two drilling operations (Figure 2a) were conducted on landslide L6 during the autumn of 2018 to test the fundamental physical properties and strength characteristics of the slide body.

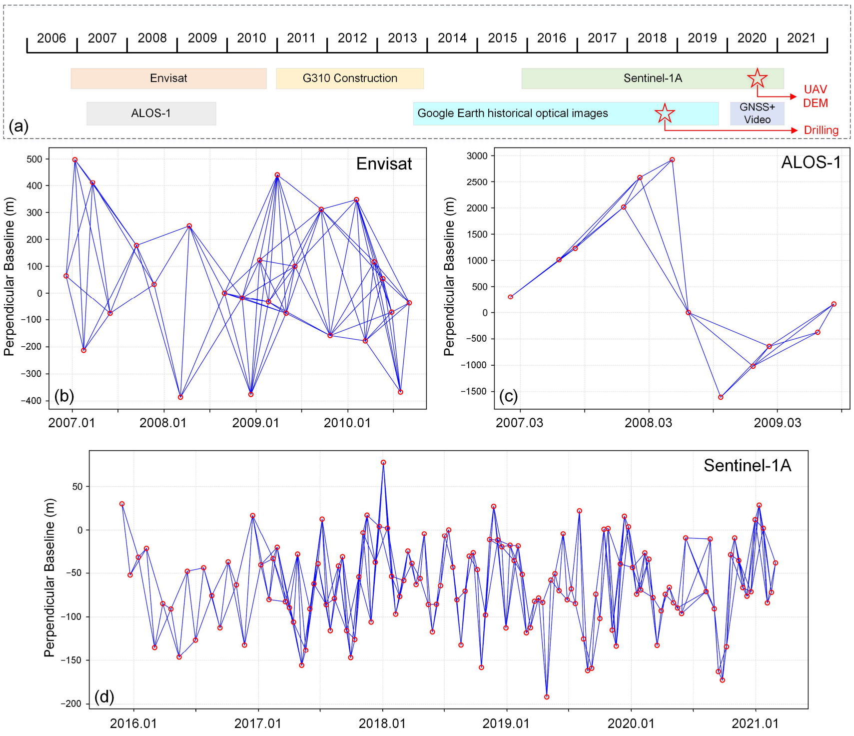

Figure 5. (**a**) Temporal coverage of SAR datasets, optical images, and GNSS observations used in this study. (**b**–**d**) Spatiotemporal baseline combinations of descending Envisat ASAR, ascending ALOS-1, and ascending Sentinel-1A datasets.

Table 1. Basic parameters of the three SAR datasets.

Sensor	Envisat	ALOS-1	Sentinel-1A
Band	C	L	C
Orbit direction	Descending	Ascending	Ascending
Polarization	VV	HH	VV
Heading (°)	−168.13	−10.26	−9.76
Incidence angle (°)	22.91	38.73	42.12
Pixel spacing (m)	7.8 × 4.0	4.7 × 3.2	2.3 × 13.9
Date range	December 2006 to September 2010	March 2007 to September 2009	November 2015 to February 2021
Number of images	26	12	138

3.2. Interferometric Processing and SBAS-InSAR Analysis

Because there are extensive farmlands and grasslands in the study area, we chose the SBAS-InSAR method to identify the maximum number of high-coherence pixels possible. This method is characterized by a redundant interferogram network that effectively reduces orbit errors and incoherent noise. Differential interference processing was performed on all SAR datasets using the GAMMA (version: 20171206) software. The generated interferogram network is shown in Figure 5. During this process, the SRTM DEM (used for the Envisat and ALOS-1 datasets) and AW3D DEM (used for the Sentinel-1A dataset) were used to simulate and remove the topographic phase. We did not perform any spectral filtering on the SAR images to preserve image resolution and maximize the density of the observation points [6].

SBAS-InSAR processing of multi-master interferograms was conducted using StaMPS software [6], which primarily involved high-coherence pixel selection, spatially uncorrelated noise correction, phase unwrapping, and spatiotemporal filtering. The amplitude dispersion index ($\leq$0.65) and pixel phase noise characteristics were combined to select the high-coherence pixels. The errors caused by the orbital ramp were modeled by using a quadratic polynomial function, and the errors resulting from topographic undulation were removed through the operation of the DEM-assisted ortho-rectification of SAR images. Generic Atmospheric Correction Online Service (GACOS) products were downloaded and adopted to correct the tropospheric delay. We applied the quadratic polynomial to estimate and remove phase ramps that may be caused by residual tropospheric or ionospheric delays and orbital errors. The wrapped phase was unwrapped using a 3D phase-unwrapping method, and spatially correlated noise was separated using an iterative filter to estimate the phase component of the deformation. Notably, during filtering, a small filtering window was selected to avoid excessive information loss. Finally, the phase component of the deformation was converted into the line-of-sight (LOS) velocity and time-series displacement using the singular value decomposition (SVD) method.

3.3. GNSS Data Processing

In January 2020, two consecutive GNSS stations (BZ02 and BZ03), equipped with Septentrio M2 receivers, were installed on the leading edge of landslide L6 (Figure 2a). As BZ03 is installed on a highly active sub-block, it is anticipated to capture a more significant deformation signal. The landslide monitoring system is constructed by integrating the GAMIT/GLOBK (version: 10.71) software, TrackRT module, and CEEMD algorithm, allowing for a near-real-time baseline solution and real-time single ephemeris solution. This system can automatically perform the entire process from real-time data acquisition to the release of monitoring results. A real-time single ephemeris solution was used in this study. For more details, please refer to Zhong et al. [32].

4. Results

4.1. LOS Displacements from December 2006 to February 2021

Figure 6a–c show the mean displacement velocities along the LOS direction of the Lashagou landslide group from December 2006 to September 2010 (Envisat), March 2007 to September 2009 (ALOS-1), and November 2015 to February 2021 (Sentinel-1A), respectively, which were used to trace the formation period of the Lashagou landslide group and the influence of the construction of the highway G310 (January 2011 to November 2013) on the spatiotemporal evolution patterns.

Prior to the construction of the highway (2006–2010), we used both the Envisat and ALOS-1 datasets to cross-validate the reliability of the InSAR displacements. The mean and standard deviation of the difference in displacement velocities between the Envisat and ALOS-1 maps for corresponding points (closest and within 50 m proximity) were determined to be 3.69 and 3.50 mm/y, respectively, indicating that they have a high degree of agreement. The observed disparity can be primarily attributed to the distinct imaging geometries of the two independent SAR datasets (Table 1). Harmonizing these datasets into the same benchmark for comparison is challenging, particularly when the geometry of the landslide movement, including its sliding direction and inclination, remains unknown [33]. In addition, the incomplete agreement between the observation periods of the Envisat and ALOS-1 datasets may also explain the above discrepancy because the displacement of landslides is typically nonlinear (e.g., Figure 7b,d,f). After the completion of the highway construction (2015–2021), we examined the InSAR measurements of Sentinel-1A using high-precision GNSS observations. As shown in Figure 7d, the time-series displacement derived from Sentinel-1A datasets using the SBAS-InSAR method exhibited a strong agreement with the GNSS (BZ02) observations, and both have highly similar displacement trends and magnitudes, with the mean and standard deviation of the differences being 5.99 and 4.42 mm/y, respectively. This slight disparity is acceptable for landslide displacement monitoring and may be because the spatial locations of the GNSS sites and the corresponding InSAR measurement points do not exactly correspond.

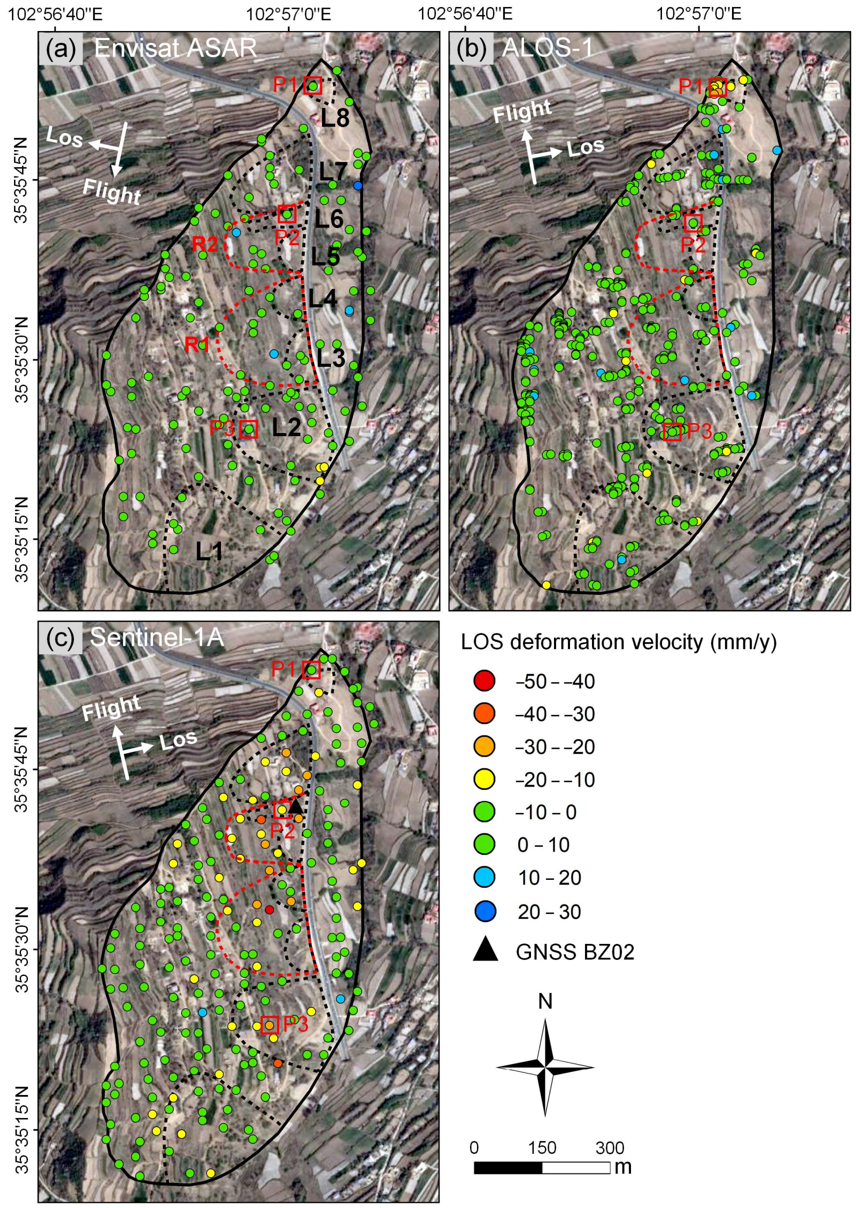

Figure 6. LOS displacement velocity maps derived from (**a**) descending Envisat images (December 2006 to September 2010); (**b**) ascending ALOS-1 images (March 2007 to September 2009); and (**c**) ascending Sentinel-1A images (November 2015 to February 2021). P1–P3 are used for time-series analysis.

As shown in Figure 6a,b, the Lashagou landslide group was in a relatively stable condition prior to the construction of highway G310, and approximately 70% of the monitored points in the Envisat displacement map have deformation magnitudes in the range of ±5 mm/y, whereas approximately 85% of the monitored points in the ALOS-1 displacement map have deformation magnitudes in the range of ±8 mm/y. Because of the large incidence angle in the ALOS-1 dataset (Table 1), the projected landslide displacement component in the LOS direction is greater. Consequently, the overall displacement magnitude measured using the ALOS-1 dataset is slightly higher than that obtained using the Envisat dataset. In addition, active landslide L8 was identified at the foot of the northeastern part of the slope with a maximum displacement velocity of −21.7 mm/y. As shown in Figure 6c, the Lashagou landslide group exhibited continuous downward movement after the construction of the highway, and most of the landslides experienced displacements exceeding 20 mm/y, either across the whole or in specific localized regions. The most severely deformed region is situated in the central part of retrogressive landslide R1, which has a maximum displacement velocity of −47.4 mm/y. In addition, under the constant traction of active landslides L5 and L6, the overlying slopes began to deform owing to the reduction in the support force, gradually forming retrogressive landslide R2.

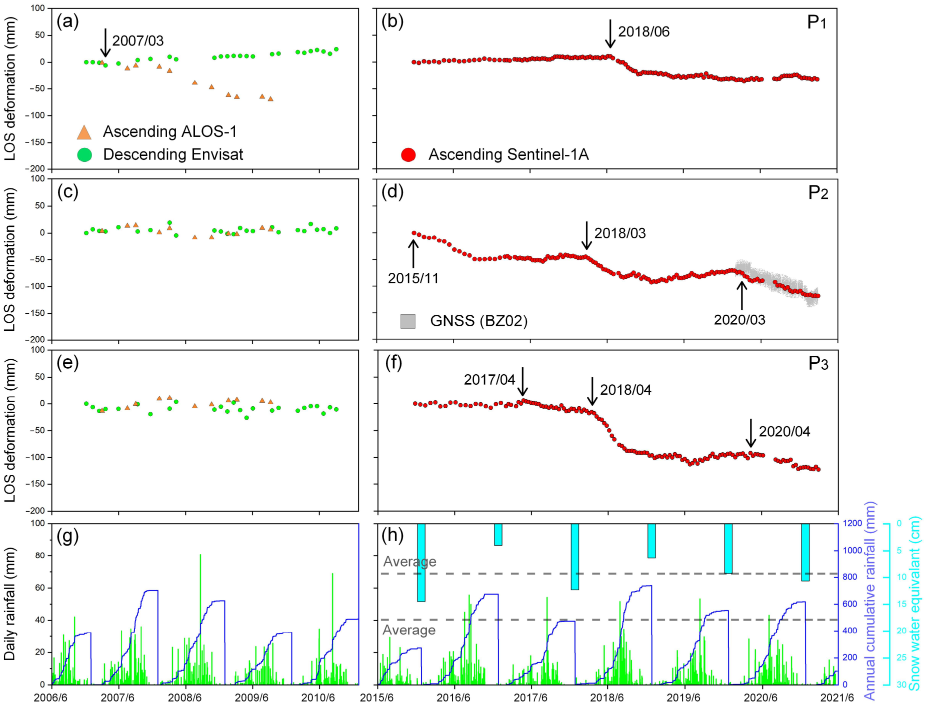

Figure 7. Time series displacement for Points P1–P3 (marked in Figure 6) from December 2006 to February 2021. (**a**,**b**) P1; (**c**,**d**) P2; and (**e**,**f**) P3. The green circles, orange triangles, and red circles represent the time-series displacement obtained from the Envisat, ALOS-1, and Sentinel-1A datasets, respectively, whereas the gray rectangles represent the GNSS (marked in Figure 6c) displacements along the LOS direction. (**g**,**h**) Rainfall and snowfall during the monitoring period, where the green line, blue line, and light blue column indicate the daily rainfall, annual cumulative rainfall, and annual cumulative snowfall, respectively. Additionally, the gray dashed line represents the average rainfall and snowfall over the last decade.

4.2. Formative Period Tracing

We traced the formation period and evolutionary history of the Lashagou landslide group by combining the InSAR time-series displacement (Figure 7) and historical optical imagery (Figure 8). Landslide formation periods were separated into three categories.

Before the construction of highway G310 (landslide L8): As shown in Figure 7a, P1 is situated at the crown of landslide L8, and the time-series displacement obtained from both the Envisat and ALOS-1 datasets indicates that landslide L8 began to deform in March 2017 and continued until September 2010. Specifically, landslide L8 had a cumulative LOS displacement of 24 mm in the descending Envisat results from December 2006 to September 2010, whereas the ascending ALOS-1 results had a cumulative LOS displacement reaching 69 mm from March 2007 to September 2009. The ratio r_1 of the cumulative LOS displacement obtained from similar time periods between the ALOS-1 and Envisat datasets was approximately 4.6 and was primarily attributed to the different imaging geometries of these datasets. Assuming that landslide L8 exhibited translational movement, we obtained its average slope aspect and gradient using the UAV DEM as the direction and inclination of the landslide displacement. Combining the imaging geometry of the Envisat and ALOS-1 datasets (Table 1), we derived the scale factors for the projection of the displacement vector of landslide L8 into the InSAR LOS direction to be 0.16 and 0.92, respectively (with a ratio

r_2 of approximately 5.75). The deviation between r_1 and r_2 is acceptable, considering the uncertainty of the translational movement assumption and InSAR measurements.

Figure 8. Historical optical images of typical landslides in the Lashagou landslide group. (**a**–**e**) Landslide L8; (**f**–**i**) Landslide L6; (**j**,**k**) Landslide L2. Optical images from 2013 to 2019 were obtained from Google Earth, whereas the image from August 2020 was a UAV-generated orthophoto.

Landslide L8 formed a through-crown tension crack prior to September 2013, as shown in Figure 8a, which allowed it to gain greater freedom of movement from the surrounding materials. Subsequently, landslide L8 continued to drag the upper slope until October 2015 when significant damage occurred (Figure 8b). Disturbed landslide L8 experienced a decrease in its gravitational potential energy and established a new state of stress equilibrium with the basal moraines. Subsequently, the landslide entered a period of stabilization from November 2015 to May 2018, was not reactivated until June 2018, and continued to deform until November 2018 (Figure 7b). Furthermore, the surface texture information obtained from historical optical imagery further confirmed that landslide L8 remained in a stable condition following the initial activity (Figure 8b,c). Additionally, localized reactivation occurred between November 2016 and October 2019 (Figure 8d). Combined with the InSAR time-series displacement (note that P1 in the Sentinel-1A map is situated outside the crown of the locally damaged sub-block, and the displacement is a result of traction from this sub-block), we can shorten the timeframe of this localized damage from June to November 2018, and landslide L8 has been stabilized since then (Figures 7b and 8e).

During the construction of highway G310 (landslides L3, L4, L5, and L6): For landslide L6, the time-series displacement at P2, situated in its center, indicates that the landslide was in a stable state until the construction of the highway (Figure 7c). During construction (before September 2013), a local collapse occurred at the foot of landslide L6 (Figure 8f), which subsequently caused progressive damage to the upper slope over time (Figure 8g). The time-series displacement derived from the Sentinel-1A dataset (Figure 7d) similarly captured the continuous downhill signal of landslide L6 after the construction of the highway (November 2015 to September 2016) and showed that the landslide was in a stabilized state between October 2016 and March 2018. Historical optical imagery showed that by October 2019 (Figure 8h), the posterolateral tensile and flank shear cracks of landslide L6 had penetrated to form a trap, indicating the complete formation of the landslide. Based on our analysis, landslide L6 underwent a severe sliding event from March 2018 to October 2019, and the InSAR time-series displacement revealed that the event occurred between April 2018 and early August 2018 (Figure 7d). Subsequently, landslide L6 transitioned to a stable state, reactivated in February 2020, and continued to deform until February 2021.

After the construction of the highway (landslides L1, L2, L7, R1, and R2): For landslide L2, the time-series displacement at P3, situated in its center, indicates that the landslide was in a stable state until the construction of the highway (Figure 7e). After construction was completed, the landslide remained stable until April 2017, when it was initially triggered and rapidly transitioned to a critical destabilization state within a year. Subsequently, in August 2018, a significant failure occurred (Figure 7f). Historical optical imagery (Figure 8j,k) documented changes in the surface morphology before and after the failure of landslide L8, which resulted in the destruction and collapse of houses at the trailing edge (Figure 2g), fragmentation of the surface, and failure of the retaining wall at the front edge (Figure 2f). The destructive event resulted in the dislocation of landslide L8 by 1–2 m without depleting its gravitational potential energy; thus, it was reactivated in April 2020 and continued its downward movement until September of the same year (Figure 7f).

5. Discussion

Following the analysis presented in Section 4.2, it was determined that the landslides within the Lashagou landslide group, with the exception of L8, were formed either during the construction of highway G310 (L3, L4, L5, and L6) or after its completion (L1, L2, L7, R1, and R2). Excavation conducted during the construction of the highway is widely acknowledged as a significant factor and an essential condition for the formation of the Lashagou landslide group (e.g., [10,24]). This excavation activity altered the original state of the stress equilibrium in the slope, thereby directly inducing slope deformation, as exemplified by the occurrence of landslide L6. Moreover, the steep free surface created by excavation deprives the slip-resistant structure of the natural slope, potentially lowering the threshold for shallow landslides triggered by rainfall [34], such as the occurrence of landslide L2.

As shown in Figure 7, the majority of landslides were activated during the snowmelt period (mid-February to early April) in 2017, 2018, and 2020, and then continued to accelerate downslope during the subsequent wet season (mid-May to early October). Therefore, snowmelt and precipitation are considered the main drivers of the continued downward movement of the Lashagou landslide group, which is consistent with the findings of Zhou et al. [30] and Zhang et al. [10]. It is worth noting that 2018 appears to be the most exceptional year of the 2006–2021 period, with landslides L3 and L4 first occurring in early April, followed by landslides L2 and L1 in their succession of total or localized failure in August. As shown in Figure 7h, the cumulative snowfall during the winter of 2017 (resulting in snowmelt in the spring of 2018) and the cumulative rainfall during the summer of 2018 were higher than the averages recorded in the last 10 years. As a result of the shallow burial depth of the sliding surface (Figure 3), a significant influx of snowmelt and precipitation infiltrated and saturated the basal shear zone of the landslide. This caused an elevation in the pore water pressure and a reduction in the soil's frictional resistance and shear strength [4,35,36], ultimately leading to the failure of the landslide. Interestingly, we observed that freeze–thaw landslides L3 and L4 occurred at the end of the snowmelt season, coinciding with a decrease in surface soil moisture (Figure 9c). This suggested that the seasonal frozen soil within the landslides was completely thawed, and the groundwater inside the landslides was rapidly discharged from the lower part of the free surface as mudflow (See Figure 10c in Zhang et al. [10]), which was elevated due to the "freezing stagnation effect" [37]. The flow and release of groundwater may cause weak structural surfaces to penetrate each other, ultimately leading to catastrophic landslides [10].

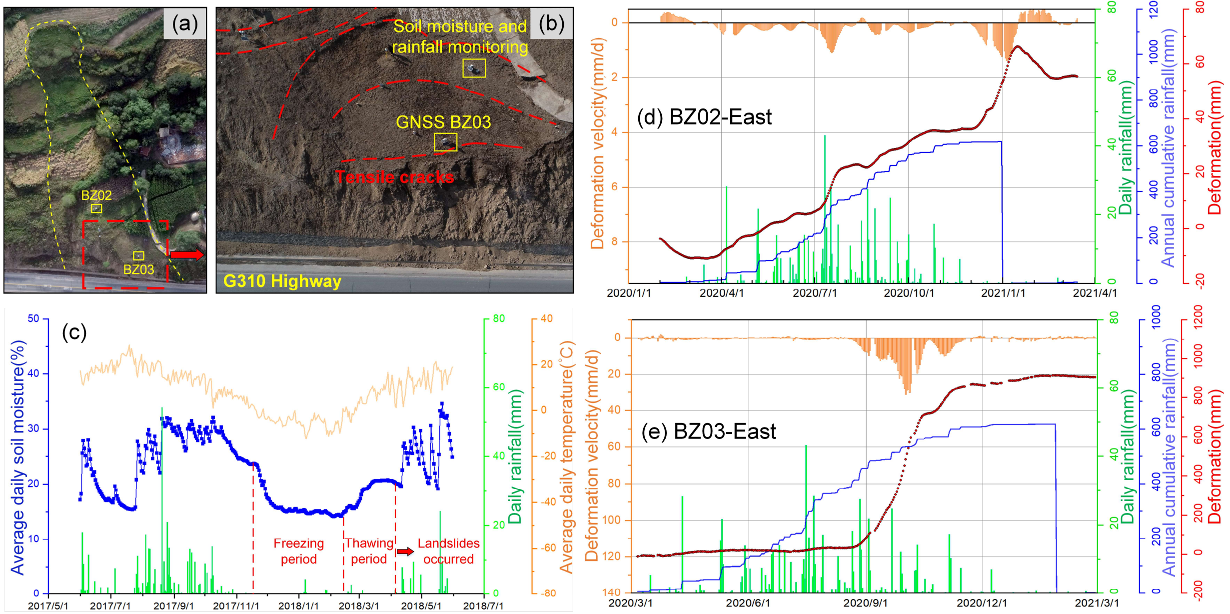

Figure 9. (**a**) Orthographic aerial photograph of landslide L6. (**b**) Locations of GNSS station (BZ03), rain gauge, and soil moisture sensor on landslide L6. (**c**) Daily rainfall (green bars), average daily temperature (orange line), and average daily soil moisture (blue dotted line) in the study area from June 2017 to June 2018. (**d**,**e**) The cumulative displacement along the E–W direction (red dotted line) and its corresponding velocity (orange bars) for BZ02 and BZ03 and compared with daily rainfall (green bars) and cumulative rainfall (blue line), respectively.

The 9-year InSAR time-series deformation provides valuable insights into the long-term displacement history of the Lashagou landslide group and facilitates the exploration of the causes and drivers contributing to its formation. However, the lower temporal resolution of InSAR measurements (typically no less than 6 d) makes it difficult to capture the rapid response of downslope movements triggered by snowmelt or rainfall. Therefore, we investigated the kinematic behavior of the Lashagou landslide group, including seasonal variations, transient acceleration events, and episodic failure events, by combining GNSS measurements with higher temporal sampling frequency. Figure 9a,b illustrate the precise positions of BZ02, BZ03, the soil moisture meter, and rain gauge on landslide L6. BZ03 was situated on a highly active sub-block in the upper part of the free surface at the foot of the slope. Consequently, BZ03 exhibited a displacement magnitude approximately 18 times greater than that of BZ02. The red scatter curves shown in Figure 9d,e represent the cumulative displacements of BZ02 and BZ03 along the east–west direction, as landslide L6 predominantly moved horizontally along that direction [10], whereas the orange bar graphs indicate the velocity changes at the corresponding times.

Both BZ02 and BZ03 began downslope movement around 25 March 2020, when snowmelt infiltrated the shear zone at the foot of the slope (Figure 2b), causing the downward sliding force to exceed the frictional resistance. During the subsequent rainy season, a significant correlation was observed between landslide displacement and cumulative rainfall (Figure 9d). This correlation indicates that both the long-term seasonal downslope movement and transient accelerated movement were predominantly influenced by rainfall. In addition, during the monitoring period, there were five heavy rainfall events, each with precipitation exceeding 25 mm/d. Among these events, 90% were associated with the transient acceleration of landslides, exhibiting an average velocity increase of 1.56 times. Moreover, the transient acceleration event of the landslide occurred on the second and first days immediately after the heavy rainfall in the dry and rainy seasons, respectively, indicating that the movement of shallow loess landslides is not only highly sensitive to rainfall intensity but is also influenced by the preceding rainfall. By calculating Pearson's correlation coefficient, our previous study [36] also demonstrated that the deformation of landslides exhibited a delay of approximately 2 days following rainfall, with a peak correlation coefficient of 0.627. Compared with most deep-seated landslides (e.g., [14,23]), the time lag of 1–2 d is short, and this is potentially related to the time required for the increase in pore water pressure to be transmitted to the basal sliding surface. Specifically, during the rainy season, the upper layer of the landslide became nearly saturated (Figure 9c), resulting in a shorter duration for the downward transfer of pore-water pressure compared to the dry season.

In addition, Figure 9e suggests that the active sub-block at the foot of landslide L6 may have been fully triggered and rapidly accelerated to a critical failure state after a cumulative rainfall of approximately 400 mm, which in turn may trigger the overall collapse of landslide L6. We also observed that the impact of rainfall on landslide movement was persistent, as landslides continued to experience slow downslope movement for a considerable period even after the conclusion of the rainy season (Figure 9d,e). Notably, both BZ02 and BZ03 exhibit abnormal and rapid downslope movements during the freezing period (mid-November to mid-February of the following year). This phenomenon may have been caused by the winter seasonally frozen layer obstructing the groundwater discharge channel connecting the interior and exterior of the slope. Consequently, groundwater concentrates inside the slopes, leading to the generation of significant hydrostatic pressure [37]. At this moment, the hydrostatic pressure within the landslide was considerably higher than the atmospheric pressure outside, resulting in a substantial pressure gradient that propelled the leading edge of the landslide to persistently move outward [33].

6. Conclusions

By integrating geomorphological interpretation using multi-temporal optical images, InSAR measurements with high spatial resolution, and continuous GNSS observations with high temporal resolution, we have traced the spatial and temporal evolution of the Lashagou landslide group over the past 15 years. Additionally, we have explored its kinematic behavior under external drivers such as rainfall and snowmelt, including seasonal variations, transient acceleration events, and episodic failure events. This study highlights the benefits of leveraging multi-source remote sensing data to investigate shallow deforming landslides, which is advantageous for the implementation of effective control and engineering interventions to mitigate potential landslide disasters. The main conclusions are as follows:

1. The formation of the Lashagou landslide group has been specifically categorized into three periods: L8 was formed before the construction of highway G310; L3, L4, L5, and L6 were formed during construction; and L1, L2, L7, R1, and R2 were formed within five years of the completion of the highway.
2. Hillslope excavation during the construction of the highway was the direct cause and prerequisite for the formation of the landslide group, whereas summer precipitation and spring snowmelt were the primary driving factors contributing to its continuous downward movement.
3. The occurrence of freeze–thaw landslides in spring may be related to the release of internal groundwater rather than the infiltration of meltwater.
4. Both the long-term seasonal downslope movement and transient acceleration events of the Lashagou landslide group were strongly controlled by rainfall, and there was a time lag of approximately 1–2 days between the transient acceleration and heavy rainfall events. More importantly, the movement of shallow loess landslides is not only highly sensitive to rainfall intensity but is also influenced by the preceding rainfall.

Author Contributions: Conceptualization, Q.F., S.Z. and Y.N.; methodology, Q.F., S.Z., J.S. and X.Z.; software, Q.F. and J.J.; validation, Q.F., S.Z., W.W. and X.L.; writing—original draft preparation, Q.F. and S.Z.; writing—review and editing, S.Z. and Y.N.; supervision, S.Z. and Y.N. All authors have read and agreed to the published version of the manuscript.

Funding: This work was financially supported by the National Key Research and Development Program of China (Grant No. 2020YFC1512000); The National Natural Science Foundation of China Projects (grant nos. 42074041 and 42307255); Shaanxi Province Science and Technology Innovation Team (Ref. 2021TD-51); The innovation team of ShaanXi Provincial Tri-Qin Scholars with Geoscience Big Data and Geohazard Prevention (2022) and the Open Project from Observation and Research Station of Ground Fissure and Land Subsidence in Ministry of Natural Resources (grant no. 2022-04).

Data Availability Statement: The data used to support the findings of this study are available from the corresponding author upon reasonable request.

Acknowledgments: We thank Andrew Hooper for sharing the StaMPS. We thank the European Space Agency (ESA) for providing the ENVISAT ASAR and Sentinel-1A datasets, the National Aeronautics and Space Administration (NASA) for providing the SRTM DEM, and the Japan Aerospace Exploration Agency (JAXA) for providing the ALOS-1 and AW3D DEM datasets.

Conflicts of Interest: The authors declare no conflicts of interest.

References

1. Xi, H.P.; Wei, M.P.; Xuan, C.Q. Analysis of landslide stability of a highway interchange section in Linxia. *Subgrade Eng.* **2022**, *6*, 220–225. [CrossRef]
2. Lacroix, P.; Bièvre, G.; Pathier, E.; Kniess, U.; Jongmans, D. Use of Sentinel-2 images for the detection of precursory motions before landslide failures. *Remote Sens. Environ.* **2018**, *215*, 507–516. [CrossRef]
3. Walton, G.; Christiansen, C.; Kromer, R.; Silaev, A. Evaluation of rockfall trends at a sedimentary rock cut near Manitou Springs, Colorado, using daily photogrammetric monitoring: Evaluation of rockfall trends at a sedimentary rock cut. *Landslides* **2023**, *20*, 2657–2674. [CrossRef]
4. Dille, A.; Kervyn, F.; Handwerger, A.L.; d'Oreye, N.; Derauw, D.; Bibentyo, T.M.; Samsonov, S.; Malet, J.P.; Kervyn, M.; Dewitte, O. When image correlation is needed: Unravelling the complex dynamics of a slow-moving landslide in the tropics with dense radar and optical time series. *Remote Sens. Environ.* **2021**, *258*, 112402. [CrossRef]
5. Liu, X.J.; Zhao, C.Y.; Zhang, Q.; Lu, Z.; Li, Z.H.; Yang, C.S.; Zhu, W.; Zeng, J.L.; Chen, L.Q.; Liu, C.J. Integration of Sentinel-1 and ALOS/PALSAR-2 SAR datasets for mapping active landslides along the Jinsha River corridor, China. *Eng. Geol.* **2021**, *284*, 106033. [CrossRef]
6. Hooper, A.; Segall, P.; Zebker, H. Persistent scatterer interferometric synthetic aperture radar for crustal deformation analysis, with application to Volcán Alcedo, Galápagos. *J. Geophys. Res. Solid Earth* **2007**, *112*, B07407. [CrossRef]
7. Bayer, B.; Simoni, A.; Schmidt, D.; Bertello, L. Using advanced InSAR techniques to monitor landslide deformations induced by tunneling in the Northern Apennines, Italy. *Eng. Geol.* **2017**, *226*, 20–32. [CrossRef]
8. Rosi, A.; Tofani, V.; Tanteri, L.; Tacconi, S.C.; Agostini, A.; Catani, F.; Casagli, N. The new landslide inventory of Tuscany (Italy) updated with PS-InSAR: Geomorphological features and landslide distribution. *Landslides* **2018**, *15*, 5–19. [CrossRef]
9. Roy, P.; Martha, T.R.; Khanna, K.; Jain, N.; Kumar, K.V. Time and path prediction of landslides using InSAR and flow model. *Remote Sens. Environ.* **2022**, *271*, 112899. [CrossRef]
10. Zhang, S.C.; Fan, Q.Y.; Niu, Y.F.; Qiu, S.C.; Si, J.Z.; Feng, Y.H.; Zhang, S.Q.; Song, Z.W.; Li, Z.H. Two-dimensional deformation monitoring for spatiotemporal evolution and failure mode of Lashagou landslide group, Northwest China. *Landslides* **2023**, *20*, 447–459. [CrossRef]
11. Costantini, M.; Ferretti, A.; Minati, F.; Falco, S.; Trillo, F.; Colombo, D.; Novali, F.; Malvarosa, F.; Mammone, C.; Vecchioli, F.; et al. Analysis of surface deformations over the whole Italian territory by interferometric processing of ERS, Envisat and COSMO-SkyMed radar data. *Remote Sens. Environ.* **2017**, *202*, 250–275. [CrossRef]
12. Wu, S.B.; Yang, Z.F.; Ding, X.L.; Zhang, B.C.; Zhang, L.; Lu, Z. Two decades of settlement of Hong Kong International Airport measured with multi-temporal InSAR. *Remote Sens. Environ.* **2020**, *248*, 111976. [CrossRef]
13. Cignetti, M.; Godone, D.; Notti, D.; Lanteri, L.; Giordan, D. Impacts on mountain settlements of a large slow rock-slope deformation: A multi-temporal and multi-source investigation. *Landslides* **2024**, *21*, 327–337. [CrossRef]
14. Xu, Y.K.; Kim, J.; George, D.L.; Lu, Z. Characterizing seasonally rainfall-driven movement of a translational landslide using SAR imagery and SMAP soil moisture. *Remote Sens.* **2019**, *11*, 2347. [CrossRef]
15. Wasowski, J.; Bovenga, F. Investigating landslides and unstable slopes with satellite Multi Temporal Interferometry: Current issues and future perspectives. *Eng. Geol.* **2014**, *174*, 103–138. [CrossRef]
16. Moretto, S.; Bozzano, F.; Mazzanti, P. The role of satellite InSAR for landslide forecasting: Limitations and openings. *Remote Sens.* **2021**, *13*, 3735. [CrossRef]
17. Xiao, T.; Huang, W.; Deng, Y.k.; Tian, W.M.; Sha, Y.L. Long-Term and Emergency Monitoring of Zhongbao Landslide Using Space-Borne and Ground-Based InSAR. *Remote Sens.* **2021**, *13*, 1578. [CrossRef]
18. Rodriguez, J.; Deane, E.; Macciotta, R.; Evans, T.; Gräpel, C.; Skirrow, R. Practical evaluation of single-frequency dGNSS for monitoring slow-moving landslides. *Landslides* **2021**, *18*, 3671–3684. [CrossRef]

19. Huang, G.W.; Du, S.; Wang, D. GNSS techniques for real-time monitoring of landslides: A review. *Satell. Navig.* **2023**, *4*, 5. [CrossRef]
20. Carlà, T.; Tofani, V.; Lombardi, L.; Raspini, F.; Bianchini, S.; Bertolo, D.; Thuegaz, P.; Casagli, N. Combination of GNSS, satellite InSAR, and GBInSAR remote sensing monitoring to improve the understanding of a large landslide in high alpine environment. *Geomorphology* **2019**, *335*, 62–75. [CrossRef]
21. Cenni, N.; Fiaschi, S.; Fabris, M. Integrated use of archival aerial photogrammetry, GNSS, and InSAR data for the monitoring of the Patigno landslide (Northern Apennines, Italy). *Landslides* **2021**, *18*, 2247–2263. [CrossRef]
22. Yang, H.Q.; Song, K.L.; Chen, L.C.; Qu, L.L. Hysteresis effect and seasonal step-like creep deformation of the Jiuxianping landslide in the Three Gorges Reservoir Region. *Eng. Geol.* **2023**, *317*, 107089. [CrossRef]
23. Hu, X.; Lu, Z.; Pierson, T.C.; Kramer, R.; George, D.L. Combining InSAR and GPS to determine transient movement and thickness of a seasonally active low-gradient translational landslide. *Geophys. Res. Lett.* **2018**, *45*, 1453–1462. [CrossRef]
24. Zhao, L.D.; Ma, X.P.; Xiang, Z.F.; Zhang, S.C.; Hu, C.; Zhou, Y.; Chen, G.C. Landslide deformation extraction from terrestrial laser scanning data with weighted least squares regularization iteration solution. *Remote Sens.* **2022**, *14*, 2897. [CrossRef]
25. Chen, B.; Song, C.; Chen, Y.; Li, Z.; Yu, C.; Liu, H.; Jiang, H.; Liu, Z.; Cai, X.; Nai, Y.; et al. Emergency identification and influencing factor analysis of coseismic landslides and building damages induced by the 2023 Ms 6.2 Jishishan (Gansu, China) earthquake. *Geomat. Inf. Sci. Wuhan Univ.* **2024**. [CrossRef]
26. Huang, G.; Jing, C.; Li, D.; Huang, X.; Wang, L.; Zhang, K.; Yang, H.; Xie, S.; Bai, Z.; Wang, D. Deformation analysis of Jishishan Mw 6.2 earthquake on the landslide hazard areas. *Geomat. Inf. Sci. Wuhan Univ.* **2023**. [CrossRef]
27. Liu, S.; He, B.; Wang, T.; Liu, J.; Cao, J.; Wang, H.; Zhang, S.; Li, K.; Li, R.; Zhang, Y.; et al. Development characteristics and susceptibility assessment of co-seismic geological hazards in Jishishan Ms 6.2 earthquake, Gansu Province. *J. Geomech.* **2024**. [CrossRef]
28. Cai, G.Z.; Yang, Z.H.; Wang, D.P.; Sun, Y.L.; Zhou, S.D. Cause analysis and defense countermeasures of geological hazards in Linxia city, Gansu Province. *J. Agric. Catastrophology* **2015**, *5*, 32–35. [CrossRef]
29. Yang, W.M.; Wan, F.P.; Ma, S.Q.; Qu, J.K.; Zhang, C.S.; Tang, H.B. Hazard assessment and formation mechanism of debris flow outbursts in a small watershed of the Linxia Basin. *Front. Earth Sci.* **2023**, *10*, 994593. [CrossRef]
30. Zhou, X.; Zhang, S.C.; Zhang, Q.; Liu, Q.; Ma, Z.M.; Wang, T.; Tian, J.; Li, X.R. Research of deformation and soil moisture in loess landslide simultaneous retrieved with ground-based GNSS. *Remote Sens.* **2022**, *14*, 5687. [CrossRef]
31. Qiang, D.X.; Ma, H.Z.; Zhu, Z.P.; Xun, Y.M. Spatial distribution and analysis of debris flow in Jishishan county of Gansu province. *Bull. Surv. Mapp.* **2022**, *7*, 107–111. [CrossRef]
32. Zhong, C.H.; Li, X.R.; Zhang, S.C.; Wang, X.Q. GAMIT/TrackRT used in landslide real-time GNSS monitoring. *Sci. Surv. Mapp.* **2022**, *47*, 57–65. [CrossRef]
33. Shi, X.G.; Zhang, L.; Zhou, C.; Li, M.H.; Liao, M.S. Retrieval of time series three-dimensional landslide surface displacements from multi-angular SAR observations. *Landslides* **2018**, *15*, 1015–1027. [CrossRef]
34. Pradhan, S.; Toll, D.G.; Rosser, N.J.; Brain, M.J. An investigation of the combined effect of rainfall and road cut on landsliding. *Eng. Geol.* **2022**, *307*, 106787. [CrossRef]
35. Iverson, R.M.; George, D.L.; Allstadt, K.E.; Reid, M.E.; Collins, B.D.; Vallance, J.W.; Schilling, S.P.; Godt, J.W.; Cannon, C.M.; Magirl, C.S.; et al. Landslide mobility and hazards: Implications of the 2014 Oso disaster. *Earth Planet. Sci. Lett.* **2015**, *412*, 197–208. [CrossRef]
36. Hu, X.; Wang, T.; Pierson, T.C.; Lu, Z.; Kim, J.; Cecere, T.H. Detecting seasonal landslide movement within the Cascade landslide complex (Washington) using time-series SAR imagery. *Remote Sens. Environ.* **2016**, *187*, 49–61. [CrossRef]
37. Kong, J.X.; Zhuang, J.Q.; Peng, J.B.; Ma, P.H.; Zhan, J.W.; Mu, J.Q.; Wang, J.; Zhang, D.; Zheng, J.; Fu, Y.T.; et al. Failure mechanism and movement process of three loess landslides due to freeze-thaw cycle in the Fangtai village, Yongjing County, Chinese Loess Plateau. *Eng. Geol.* **2023**, *315*, 107030. [CrossRef]